

1 Millikelvin-precision temperature sensing for advanced
2 cryogenic detectors

3 M. Antonova^a, J. Capó^a, A. Cervera^a, P. Fernández^{a,2}, M. Á. García-Peris^{a,1,*}, X.
4 Pons^b

^a*Instituto de Fisica Corpuscular Catedratico Jose Beltran 2 E-46980 Paterna (Valencia) Spain*

^b*CERN Espl. des Particules 1 1211 Meyrin Switzerland*

5 **Abstract**

Precise temperature monitoring —to the level of a few milli-Kelvin— is crucial for the operation of large-scale cryostats requiring a recirculation system. In particular, the performance of Liquid Argon Time Projection Chambers —such as those planned for the DUNE experiment— heavily relies on proper argon purification and mixing, which can be characterized by a sufficiently dense grid of high-precision temperature probes. In this article, a novel technique for the cross-calibration of Resistance Temperature Detectors (RTDs) in cryogenic liquids (argon and nitrogen) is presented, obtaining an unprecedented precision of 2.5 mK.

6 *Keywords:* Detectors, Liquid Argon, Cryogenics, Temperature, RTD, Purity,
7 Computational Fluid Dynamics

8 **1. Introduction**

9 Precise temperature sensing is essential in large cryogenic detectors, where the circulation
10 and purification of cryogenic liquids significantly impact overall detector performance.
11 Uncontrolled temperature gradients in such systems can disrupt the cryostat dynamics
12 and ultimately affect the experiment's physics sensitivity. In this work, we present the
13 calibration procedure of a novel temperature monitoring system developed for a prototype
14 of the future DUNE experiment.

*Corresponding author

Email address: miguel.garcia-peris@manchester.ac.uk (M. Á. García-Peris)

¹now in the University of Manchester

²now at Donostia International Physics Center, DIPC

DUNE, which stands for Deep Underground Neutrino Experiment [2], is expected to begin taking data toward the end of the decade. It aims to perform comprehensive neutrino oscillation analyses —broadly exploring the Charge-Parity (CP) violation parameters phase-space and resolving the neutrino-mass hierarchy problem [6]. Its extensive physics program also includes searches for hypothetical proton decay channels [3], multi-messenger astronomy from supernovae and neutrino bursts [8], and explorations of Beyond the Standard Model (BSM) physics [7]. With the most powerful neutrino beam ever built, produced at Fermilab, the experiment follows the long-baseline neutrino oscillations approach, with two detectors. The Near Detector, also at Fermilab, will characterize the unoscillated neutrino beam. The Far Detector (FD), located in the Sandford Underground Research Facility (SURF), 1300 away from the ND and 1.5 km underground, will measure the oscillated flux.

DUNE phase I far detector will have two Liquid Argon Time Projection Chambers (LArTPC), and is expected to operate by 2029. DUNE phase II will complement with two more modules by mid 30's, aiming at a total fiducial mass of 40 kilotonnes. The detector technology has been established, with excellent tracking and calorimetric capabilities, in several smaller-scale experiments [10, 13]. The first demonstration of the technology at the kilotonne scale has been carried out at the CERN Neutrino Platform as part of the ProtoDUNE program. In particular, the ProtoDUNE Single-Phase (SP) experiment [1] reproduced the detector components of the second DUNE FD module [4] at a scale 1:1 with a total argon mass 20 times smaller (770 tonnes). It was operated from mid-2018 to mid-2020, constituting the largest monolithic LArTPC to be built and operated up to date [5, 9].

During ProtoDUNE-SP operation, the level of impurities was kept way below 100 ppt oxygen equivalent using a cryogenic recirculation and purification system [1, 9]. This is fundamental in a LArTPC, as the 3D images produced by charged particles traversing the detector can be exponentially attenuated by medium impurities such as nitrogen, oxygen and water, biasing the energy measurements by absorbing ionization electrons. Three purity monitors, based on the ICARUS design [25], were installed outside the active volume of the TPC to measure the electron lifetime, which is inversely related to the residual concentration of impurities. They ran twice a day to monitor the argon

46 purity and thus to provide the necessary corrections for posterior data analysis.

47 Achieving the necessary argon purity has been possible thanks to the studies based
48 on computational fluid dynamic (CFD) simulations, and the experience gained with
49 previous LArTPC demonstrators such as LAPD [11] and the 35-tonne prototype [12, 18],
50 which have paved the way to operate large-scale cryostats requiring low concentrations
51 of impurities. These studies have also shown that it exists a strong correlation between
52 temperature and purity in the liquid argon volume. The distribution of impurities is
53 insensitive to small ($\mathcal{O} \sim 1$ K) absolute temperature variations, but strongly depends on
54 the relative vertical temperature gradient. As the bulk volume in the cryostats needs to
55 be continuously mixed with the incoming purified argon to ensure the purification of the
56 whole LAr volume, the temperature distribution acts as a clear indicator of that mixing: a
57 homogeneous temperature distribution indicates that the liquid is being properly mixed,
58 whereas large temperature gradients constitute a clear symptom of deficient mixing. If
59 the LAr bulk volume is not mixed appropriately, a stratification regime can develop: a
60 significant portion of the liquid remains unpurified, generating ‘dead’ regions inside the
61 detector. Hence, a constant monitoring of this temperature gradient can identify and
62 mitigate potential failures of the purification system. In ProtoDUNE-SP, this gradient
63 was predicted to be about 15 mK by the CFD simulations [1, 4].

64 The CFD simulations also predict, in spite of homogeneous mixing, that the con-
65 centration of impurities may also vary across the cryostat volume, requiring a position-
66 dependent electron lifetime correction. The Purity Monitors themselves are intrusive
67 objects which cannot be deployed inside the active volume, rather in only a few well-
68 defined locations near the cryostat walls; thus, precise inference of the electron lifetime
69 map requires alternative methods, as the one proposed in this article. A net of tem-
70 perature sensors cross-calibrated to the <5 mK level should allow the measurement of
71 a 15 mK temperature gradient, which can be used to constraint CFD simulations, pro-
72 viding a data-driven prediction of the impurity concentration. The main limitations of
73 this new approach are the precision of the cross-calibration of the temperature sensors
74 and the accuracy of the simulations. In this article, precise temperature monitoring for
75 ProtoDUNE-SP will be described with particular emphasis on sensor calibration.

76 **2. The temperature monitoring system of ProtoDUNE-SP**

77 ProtoDUNE-SP [1] was the Single-Phase demonstrator of DUNE Far Detector second
78 module [4], currently known as Horizontal Drift (HD) module. The elements constitut-
79 ing the TPC, its associated readout electronics and the photon detection system, were
80 housed in a 8x8x8 m³ cryostat that contained the LAr target material. The cryostat,
81 a free-standing steel-framed vessel with an insulated double membrane, is based on the
82 technology used for liquefied natural gas storage and transport. A cryogenic system main-
83 tains the LAr at a stable temperature of about 87 K, and ensures the required purity
84 level by means of a closed-loop process that recovers the evaporated argon, recondenses
85 it, filters it, and returns it to the cryostat, keeping the LAr level at about 7.3 m from the
86 bottom membrane. ProtoDUNE-SP was exposed to a charged particle test-beam from
87 October to November 2018, and later recorded cosmic rays until January 2020 [5, 9]. It
88 was finally emptied and decommissioned in Summer 2020.

89 In order to understand the LAr behaviour inside the cryostat and validate the CFD
90 simulations, 92 high-precision temperature sensors were installed inside ProtoDUNE-
91 SP, near the active volume. These sensors were distributed in two vertical arrays, or
92 Temperature Gradient Monitors (TGM), and two horizontal grids below and above the
93 TPC, respectively. Three elements were common to all systems: sensors, cables and
94 readout electronics. RTD technology [22] was chosen for this application. It consists of a
95 metallic element whose resistance changes with temperature. This resistance is measured
96 by feeding the RTD with a known current and measuring the resulting voltage. Based on
97 previous experience from other prototypes [12], Lake Shore PT102 platinum sensors [21]
98 with 100 ohms resistance at room temperature were chosen. Sensors were mounted on
99 a 52x14 mm² PCB with an IDC-4 connector, such that they could be plugged-in at any
100 time. Several versions of the PCB have been explored, finally converging to the one
101 shown in Fig. 1, which minimizes the contact of the sensor with the PCB while keeping
102 the sensor protected.

103 A careful choice of the readout cable and the connections are essential to obtain the
104 required temperature precision. See for example Ref. [22] for a detailed description. A
105 custom cable made by Axon [14] was used. It consists of four American Wire Gauge
106 (AWG) 28 teflon-jacketed copper wires, forming two twisted pairs, with a metallic ex-

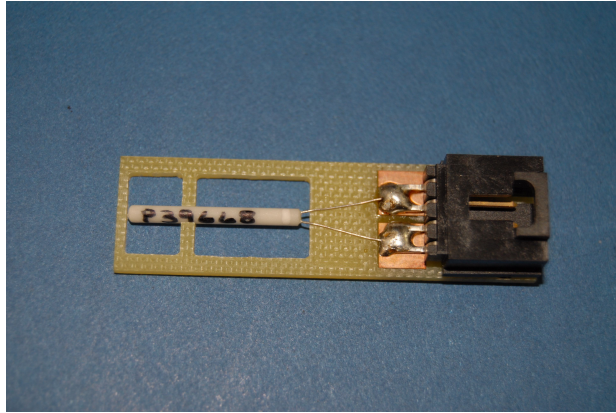


Figure 1: PCB support with temperature sensor and IDC-4 connector. The transition from two wires at the sensor to 4 wires at the readout is clearly seen. The sensor has a length of 2 cm.

107 internal shield and an outer teflon jacket. The outer diameter of the cable is 3.7 mm.
 108 Teflon was chosen for its good thermal properties and low out-gassing. The metallic
 109 external shield (connected to the readout in one end and left floating at the sensor's end)
 110 and the twisted pairs are crucial to reduce the effect of external electromagnetic noise
 111 pickup. When RTDs are far from the voltmeter, the resistance of cables and connectors
 112 are added to the one of the sensor, biasing the temperature measurement. This bias can
 113 be subtracted to some level, but cannot be fully controlled since the resistance of those
 114 elements also depends on temperature. To minimise the impact of this effect a four wire
 115 readout is introduced [22], such that the voltage is measured in the vicinity of the RTD.

116 The last common element is the readout system, consisting of a very precise 1 mA
 117 current source to excite the sensors and a 24 bits ADC to measure the voltage. The
 118 readout system will be described in detail in Section 3.

119 As previously mentioned, ProtoDUNE-SP CFD simulations predict vertical temper-
 120 ature gradients as low as 15 mK [1]. A relative precision better than 5 mK was required
 121 to validate and tune those simulations with sufficient confidence. Three main ingredients
 122 are necessary to obtain such a precision: i) high quality and stable temperature probes,
 123 ii) a very precise readout system, and iii) a precise calibration, both for the readout
 124 and the sensors. As mentioned above, two TGMs were deployed in ProtoDUNE-SP: one
 125 could be moved vertically and hence calibrated *in situ*, while the other one —static—

126 fully relied on a prior calibration in the laboratory. In this article, the calibration of the
127 static TGM [17] sensors is described in detail. This device consists of a vertical array of
128 48 sensors, installed 20 cm away from the lateral field cage.

129 The calibration was performed once in spring 2018 (a few months before the operation
130 of ProtoDUNE-SP), and several times after ProtoDUNE-SP decommissioning. In this
131 article the calibration setup, procedure and results will be described in detail. Compar-
132 ison between the different calibration campaigns will be addressed, revealing important
133 information about systematic uncertainties and RTD ageing.

134 3. Readout system

135 A precise and stable electronic readout system is needed to achieve the required precision.
136 In previous versions of the calibration system, each sensor was connected to a different
137 and independent electronic circuit and thus, fed by a different current and read by a
138 different ADC channel. It was soon realized that the measured temperature difference
139 between any two pairs of sensors was heavily affected by the electronic offset between
140 channels. This offset was not constant, and showed dependence on ambient temperature
141 and humidity, which affected both the current source and the ADC, generating variations
142 of tens of mK for the measurement of a single calibration constant between sensors. A
143 variant of an existing mass PT100 temperature readout system developed at CERN for
144 one of the LHC experiments [16] was adapted to solve this problem. The system consists
145 of an electronic circuit that includes:

- 146 • A precise and accurate 1 mA current source for the excitation of the temperature
147 sensors based on an application of the Texas Instruments precise voltage reference
148 REF102CU with a possibility to adjust $\pm 10\text{nA}$ with Keithley 2001 multimeter [15,
149 23].
- 150 • A multiplexing circuit based on the Analog Devices ADG1407BRUZ multiplexer
151 with ultralow internal resistance in an 8-channel differential configuration. The
152 readout circuit contains three multiplexers, providing a readout capacity of 24
153 channels. The multiplexing circuit and the current sourced are realised in a single
154 card (see Fig. 2).

- 155 ● A readout system based on National Instruments Compact RIO-FPGA device [19]
 156 equipped with a NI-9238 analogue input module that provide 24 bits of resolution
 157 over 1 volt range [20]. By programming the Van Dusen equation the readout
 158 calculates the temperature in Kelvin units. The Compact RIO also drives the
 159 control bits of the multiplexers

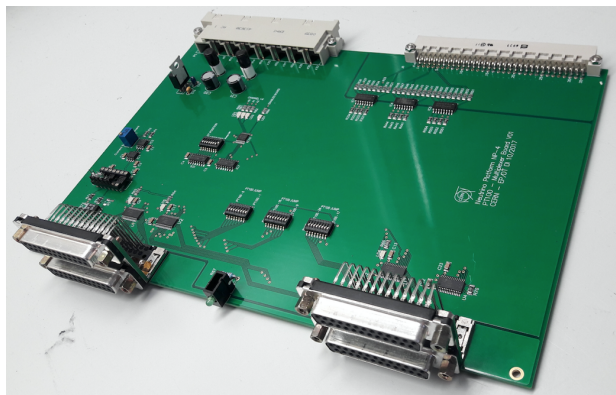


Figure 2: Current source and multiplexing card with 24 channels.

160 One of the features of the readout circuit is the serialization of the current source exci-
 161 tation for all the sensors connected to the same board, such that the same 1 mA current
 162 is delivered to all of them. Multiplexing the signal of the sensors such that they can be
 163 readout by the same ADC channel minimises the residual offset due to the electronics.
 164 This system was used during the calibration campaigns presented in this article and also
 165 for the temperature measurements during ProtoDUNE-SP operation.

166 The readout was not considered a potential source of bias during the calibration
 167 campaign prior to the installation in ProtoDUNE-SP (see Sec. 4) and it was not stud-
 168 ied in detail at that time. However, aiming to improve the calibration results after
 169 ProtoDUNE-SP operation, a more thoughtful study of the readout was performed before
 170 the calibration campaigns presented in Sec. 5. In particular, the twelve channels (7-18)
 171 used for sensor calibration were investigated. It was found that, despite the multiplexing
 172 system, a small residual offset between channels still exists. Fig. 3 shows the offsets of
 173 channels 8-18 with respect to channel 7, computed using twelve 20 ohms low Temperature

174 Coefficient of Resistance (TCR)³ precision resistors, with an equivalent temperature of
 175 76 K. Two of those, High Precision 1 (HP1) and High Precision 2 (HP2), are selected as
 176 the measurement samples and connected to the reference channel (7) and the channel be-
 177 ing calibrated (from 8-18), while leaving all other channels connected to other secondary
 178 resistors to let the current flow through the system. The readout offset between chan-
 179 nel 7 and channel X, $\Delta T_{7-X}^{readout}$, is then computed using the results of two consecutive
 180 measurements:

- 181 1. HP1 in channel 7 and HP2 in the channel X being calibrated. The offset between
 182 the measured temperatures is

$$\Delta T_{7-X}^A = T_X^{HP2} - T_7^{HP1} + \Delta T_{7-X}^{readout}. \quad (1)$$

- 183 2. HP2 channel 7 and HP1 in the channel X being calibrated. The offset between the
 184 measured temperatures is

$$\Delta T_{X-7}^B = T_X^{HP1} - T_7^{HP2} + \Delta T_{7-X}^{readout}. \quad (2)$$

185 Because of the very low TCR of the resistors, it can be assumed that the resistances
 186 are constants in those two measurements ($T_7^{HP1} = T_X^{HP1}$ and $T_7^{HP2} = T_X^{HP2}$). Thus,
 187 the offset between channels 7 and X can be computed as the average between those two
 188 measurements:

$$\Delta T_{7-X}^{readout} = \frac{\Delta T_{7-X}^A + \Delta T_{X-7}^B}{2}. \quad (3)$$

189 The results in Fig. 3, show an offset of up to 2.5 mK when comparing directly with
 190 channel 7, while the offset between any other two channels is below 1 mK, indicating that
 191 there is something special about the first channel being readout. Error bars in that figure
 192 correspond to the standard deviation of four independent measurements (repeatability)
 193 of the same offset (see Fig. 3). As it can be observed the error is below 0.5 mK, what
 194 probes the great repeatability of the readout. These offsets are more likely due to parasitic

³The temperature coefficient of resistance is defined as the change in resistance per unit resistance per degree rise in temperature. Typically $\pm 5\text{ppm}/^\circ\text{C}$.

195 resistances in the different lines that are multiplexed. This finding allowed a correction
 196 to the measurements taken during the subsequent calibration campaigns, improving the
 197 obtained precision.

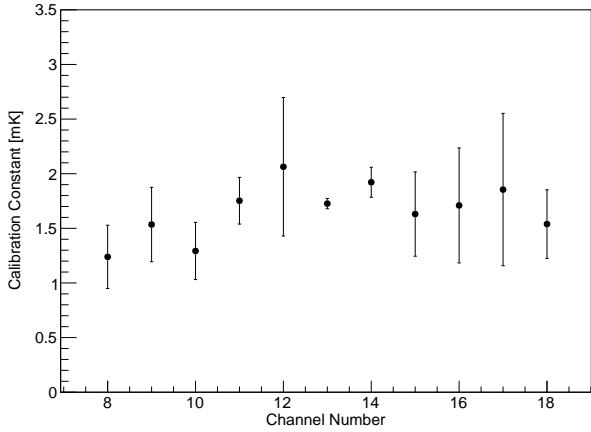


Figure 3: Offset between readout channels 8-18 and channel 7, used as reference. Points correspond to the mean of the 4 independent measurements and the error bars are their standard deviation.

198 **4. Calibration before the installation in ProtoDUNE-SP**

199 The Lake Shore Cryotronics company provides PT102 RTDs with a temperature reading
 200 dispersion of about 0.1 K, which is insufficient for ProtoDUNE-SP's requirements. While
 201 the company offers additional calibration to the 10 mK level, the cost is prohibitive.
 202 R&D on sensor calibration was identified as a crucial ingredient for the success of the
 203 ProtoDUNE-SP temperature monitoring system. For this particular application, sensor
 204 calibration consists in finding the temperature offset between any pair of sensors when
 205 exposing them to the same temperature. The experimental setup used for the calibration
 206 of RTDs before their installation in ProtoDUNE-SP had two main components: i) the
 207 readout system used to monitor the sensor's temperature (described in the previous
 208 section) and ii) the cryogenics vessel and the associated mechanical elements used to put
 209 sensors together under stable cryogenics conditions. They were developed to achieve a
 210 relative calibration with a precision better than 5 mK.

211 *4.1. Experimental setup*

212 The mechanics of the calibration setup evolved significantly from the initial tests to the
213 final Static TGM calibration. This evolution was primarily driven by the need to improve
214 offset stability and repeatability. The final configuration (see Fig. 4) consisted of the
215 following components:

- 216 • A polystyrene vessel formed by an outer box with dimensions $35 \times 35 \times 30 \text{ cm}^3$ and
217 4.5 cm thick walls, and a dedicated polystyrene cover, complemented by extruded
218 polystyrene panels glued into the inner walls and floor of the outer box, to conform
219 an inner empty volume of $10 \times 10 \times 20 \text{ cm}^3$.
- 220 • A $10 \times 10 \times 20 \text{ cm}^3$ 3D printed polylactic acid (PLA) box with two independent con-
221 centric volumes, placed in the inner volume of the polystyrene vessel. Its purpose
222 is twofold: i) to contain LAr, since polystyrene is porous to it, and ii) to create an
223 smaller inner volume with further insulation and less convection.
- 224 • A cylindrical aluminum capsule, to be placed in the inner volume of the PLA box,
225 with 5 cm diameter, 12 cm height and 1 mm thin walls. It had a circular aluminum
226 cover with a small opening to extract the cables and to allow LAr to penetrate
227 inside. The capsule was used to slowly bring sensors to cryogenic temperatures by
228 partial immersion in LAr with no liquid inside, minimizing thermal stress. Alu-
229 minum was chosen for its high thermal conductivity.
- 230 • A 3D printed PLA support for four sensors, to be placed inside the aluminum
231 capsule, keeping sensors always in the same position with respect to each other and
232 to the capsule walls.

233 The system described above provides stable conditions in the inner volume, with
234 three levels of insulation: the outer polystyrene vessel and two PLA box LAr volumes.
235 The aluminium capsule is key to this system and its usage constituted a turning point in
236 the R&D since it minimises thermal shocks, which were identified as the main limiting
237 factor for the repeatability of the sensor's offsets. Indeed, variations of several tenths
238 of mK were observed in initial tests without the capsule. The problem was attributed
239 to thermal shocks when, after many immersions in LN₂, one of the sensors suffered a

²⁴⁰ dramatic change in its offset (see Fig. 5). Examination at the microscope revealed cracks
²⁴¹ in the outer RTD ceramics (see Fig. 6).



Figure 4: Final calibration setup. Left: polystyrene box with PLA box and aluminum capsule. Middle: aluminum capsule. Right: Sensor's support with four sensors.

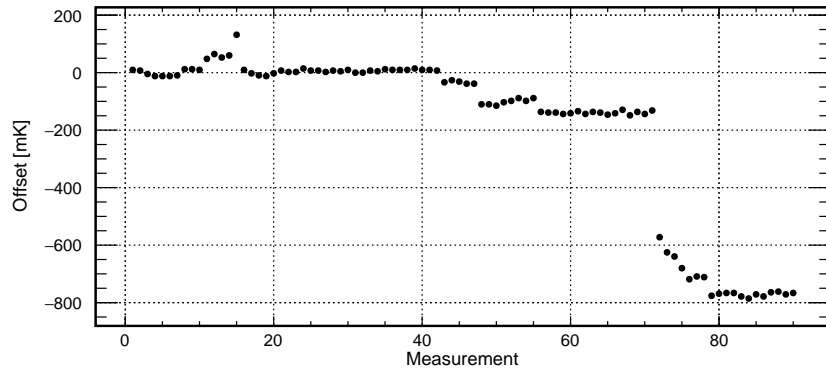


Figure 5: Offset between two sensors for 90 immersions in LN₂. A drop of 800 mK is observed.

²⁴² 4.2. Calibration procedure

²⁴³ The calibration procedure relies on the assumption that all sensors in the capsule are at
²⁴⁴ the same temperature. This limits the number of RTDs in a single run to four, since
²⁴⁵ i) they should be as close as possible to each other and ii) as far as possible from the
²⁴⁶ capsule walls (the sensor closer to the wall could be biased). Two different methods,
²⁴⁷ described schematically in Fig. 7, were used to cross-calibrate all 48 sensors in runs of 4
²⁴⁸ sensors:

²⁴⁹ 1. **Reference method:** all sensors are calibrated with respect to a reference one, in
²⁵⁰ sets of three sensors (the fourth one would be the reference sensor, which must be
²⁵¹ present in all runs). In total there are sixteen calibration sets.

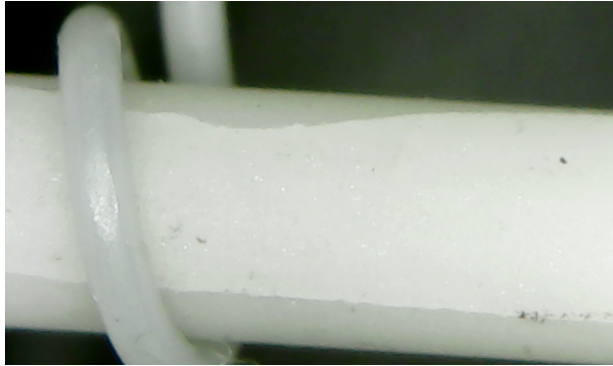


Figure 6: Cracks observed with the microscope in the ceramic of the sensor.

252 **2. Tree method:** Four different sets of sensors can be cross-calibrated by performing
 253 a second round of measurements with a single promoted sensor from each of those
 254 four sets. Since there are 16 sets in total, a third round of measurement is needed
 255 to cross-calibrate the four sets in the second round.

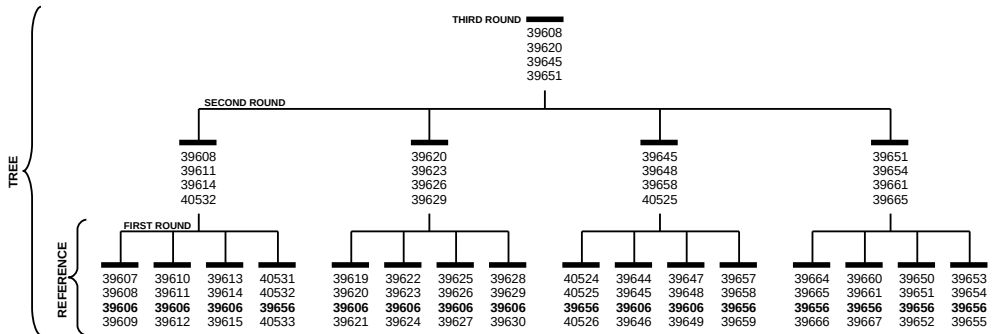


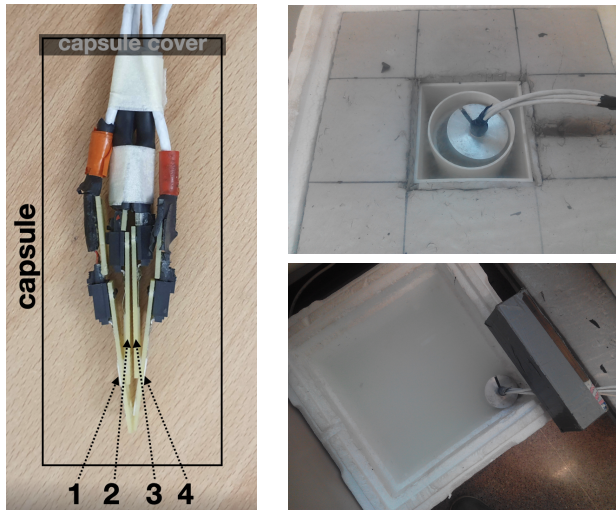
Figure 7: Schematic view of calibration sequence. Each number represents a different RTD, and the numbers in bold represent the reference sensors. The first round consists on a direct calibration respect to a reference sensor. The second and third rounds are needed to relate all sensors independently of the reference sensor.

256 The reference method was expected to be more precise since any two sensors were
 257 related through a single intermediate sensor (the reference one), while for the tree method
 258 the relation between any two sensors required more than one intermediate sensor. For
 259 example, the offset between sensors i and j in different sets, related through sensors k
 260 and l in the second round, would be $\Delta T_{ij} = \Delta T_{ik} + \Delta T_{kl} + \Delta T_{lj}$. For sensors related
 261 through the third round an additional term should be added, further increasing the offset

262 uncertainty.

263 Offset repeatability is a critical parameter to understand, as the laboratory calibration
264 must remain valid when applied to the actual detector. To study this, four independent
265 calibration runs were performed for each set of four sensors. However, due to concerns
266 about thermal fatigue in the primary reference sensor—subjected to 64 thermal cycles
267 over the four repeatability runs—three secondary reference sensors were employed to
268 regularly monitor its response and ensure reliability over time.

269 The following procedure is applied for each set of four sensors. First, they are placed
270 inside the aluminium capsule. The sensor with the highest serial number is placed in the
271 orange connector, and the one with the lowest in the red. The central connector closer to
272 the red one is used for the reference sensor. These positions are easily called by numbers
273 from 1 (orange) to 4 (red), as shown in Fig. 8-left.



274 Figure 8: Left: Picture of sensor order inside the flask. Position 1 corresponds to highest serial number
275 and 4 to lowest; position 3 is reserved to reference sensor. Top: Flask partially introduced in LAr.
276 Bottom: Flask partially introduced in room water to warm up sensors before performing a new measurement.

277 After filling the PLA box with LAr, the aluminum capsule is partially immersed (see
278 Fig. 8-right-top) such that the air inside cools-down slowly, avoiding direct exposure
279 of the sensors to LAr, which would result in a thermal shock. When the monitored
280 temperature approaches the one of LAr (< 95 K), which takes about 15 minutes, the
281 capsule is completely immersed, being filled with liquid. The PLA box is then completely

279 filled with LAr to account for evaporation during the cool-down phase. Finally, the
280 polystyrene vessel is closed using the polystyrene lid. The actual calibration runs for
281 forty minutes.

282 When the measurement is finished, the capsule is extracted from the liquid, emptied
283 of LAr and partially immersed into another polystyrene box filled with water at room
284 temperature (see Fig. 8-right-bottom). The warm-up process takes about ten minutes.
285 When sensors have reached a temperature around 250 K a new independent measurement
286 can start.

287 Fig. 9 shows the typical evolution of the temperature for the four sensors in the
288 capsule during the warm-up and cool-down processes. A sudden fall to 87 K is observed
289 at minute 32, which corresponds to total immersion of the sensors in LAr. Notice also
290 that two of the sensors have lower temperature during the cool-down process; those are
291 sensors 1 and 4, the ones closer to the capsule walls.

292 For each set of sensors the procedure described above is repeated four times, resulting
293 in four independent measurements of the same offset. These measurements are used to
294 compute a mean offset value and its standard deviation (repeatability from now on).

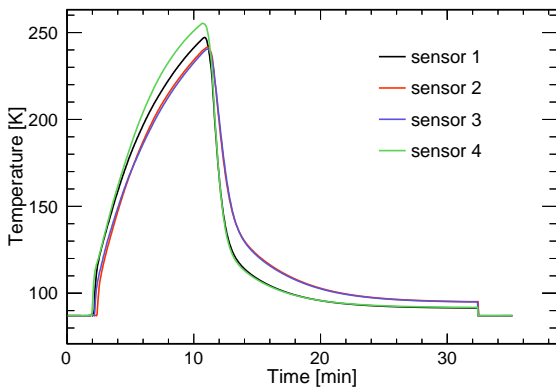


Figure 9: Temperature evolution during the warm-up and cool-down processes between two consecutive runs.

295 *4.3. Calibration results*

296 Here we present the results of the calibration using both calibration methods, a study of
297 the consistency of these results, and a preliminary estimation of the systematic uncer-
298 tainty of the calibration process.

299 *4.3.1. Results on the first round of measurements*

300 Fig. 10 shows the offset of three different sensors with respect to the reference sensor as
301 a function of time, and for four independent calibration runs. The offset is more stable
302 for the sensor closer to the reference (position 2), while external sensors (positions 1
303 and 4) have larger variations, but present similar patterns between them. This effect
304 is attributed to the geometry of the system, with sensors at different heights and not
305 symmetrically positioned with respect to the capsule walls, and was taken into account
306 when developing the second version of the system, presented in Sec. 5.

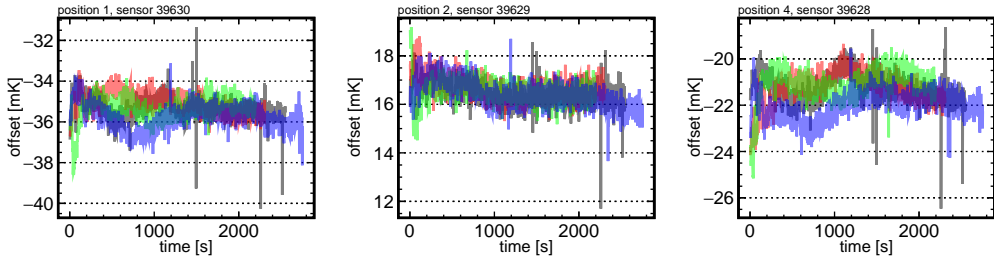


Figure 10: Offset between the reference sensor and each of the three sensors in a set, as a function of time. Each colour represents an independent measurement.

307 The mean offset for each sensor and each calibration run is calculated as the average
308 over the time interval between 1000 and 2000 seconds, identified as the most stable
309 region for the majority of sensors. The standard deviation of the four measurements is
310 taken as the uncertainty, hereafter referred to as repeatability. As shown in Fig. 11, the
311 uncertainties are generally below 1 mK, demonstrating the high level of repeatability
312 achieved in the calibration process.

313 *4.3.2. Time walk correction for reference sensors*

314 Time evolution of the response of sensor 39606 was studied by periodically (every \sim 20 im-
315 mersions) computing its offset with respect to three secondary reference sensors, 39603,
316 39604 and 39605. For each of those additional calibrations, two runs were taken in-
317 stead of four in order to minimize thermal fatigue of the reference sensor. As shown
318 in Fig. 12-left, the offset, computed as the mean of those two runs, varies linearly at a
319 rate of 0.07 mK/immersion, which suddenly increases to 0.22 mK/immersion after 60
320 runs. This change in the slope may be related with the frequency of immersions, which
321 increased from 3/day to 5/day. Sensor 39606 was initially used for other purposes, and

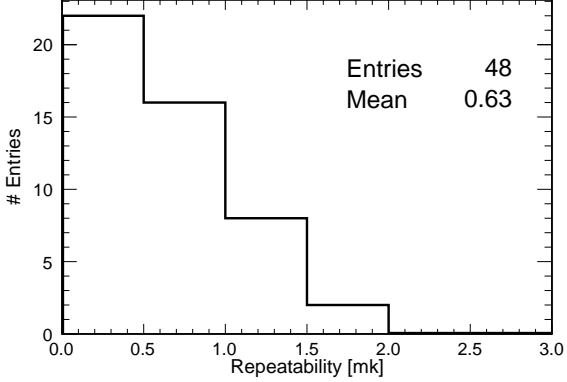


Figure 11: Distribution of the repeatability for calibration runs in the first round.

322 the calibration of the 48 sensors conforming the static TGM started approximately at
 323 immersion 40. Given this change in its response, sensor 39606 was substituted by 39656
 324 as primary reference for the last quarter of the TGM calibration in order to avoid further
 325 fatigue and potential untraceable behaviour. The evolution of the new reference sensor
 326 is shown in Fig. 12-right. It is worth noting that the same slopes are valid for the three
 327 secondary reference sensors in both cases, supporting the idea that the change observed
 328 in the offsets can be exclusively attributed to thermal fatigue of the reference sensor.

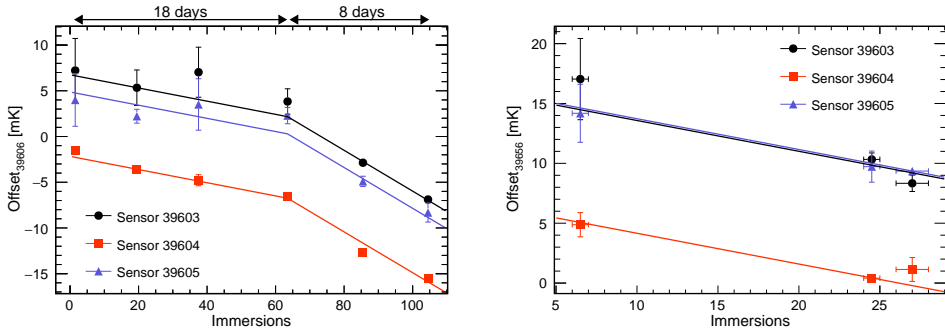


Figure 12: Offset between the reference sensors (39606 on the left panel and 39656 on the right panel) and the three secondary references as a function of the number of immersions. Offsets for sensor 39604 have smaller errors because of its position inside the capsule. Solid lines correspond to the parametrization in Eq. 4.

329 The zero intercept in both panels of Fig. 12 corresponds to the unbiased offset (or the
 330 offset at $N_{\text{immersions}} = 0$) of each of the secondary reference sensors with respect to the

³³¹ primary reference. In order to compute the unbiased offset for a sensor s , a time walk
³³² correction after N immersions is calculated as

$$\Delta T_{s,06}(N = 0) = \begin{cases} \Delta T_{s,06}(N) + (0.072 \pm 0.003) * N & N < 63.5 \\ \Delta T_{s,06}(N) + (0.072 \pm 0.003) * 63.5 + \\ \quad +(0.223 \pm 0.007) * (N - 63.5) & N > 63.5, \end{cases} \quad (4)$$

$$\Delta T_{s,56}(N = 0) = \Delta T_{s,56}(N) + (0.168 \pm 0.007) * N. \quad (5)$$

³³³ All sensors can be related to the same primary reference sensor, 39606, adding the
³³⁴ unbiased offset between sensors 39606 and 39656, $\Delta T_{56,06}(N = 0)$, to sensors calibrated
³³⁵ with respect to 39656. By averaging over the three secondary reference sensors, the value
³³⁶ obtained is $\Delta T_{56,06}(N = 0) = -9.19 \pm 0.13$ mK.

³³⁷ 4.3.3. Results on the reference method

³³⁸ Fig. 13 shows the offset of all sensors with respect to the 39606 reference. As it can
³³⁹ be noticed, the dispersion of the offsets is compatible with 0.1 K, the value quoted by
³⁴⁰ the vendor. Fig. 14-left shows the distribution of the repeatability of the computed
³⁴¹ calibration constants after applying the different corrections, showing an average value
³⁴² below 1 mK.

³⁴³ 4.3.4. Results on the tree method

³⁴⁴ The offsets are computed in this case with respect to an arbitrary reference among all
³⁴⁵ sensors being calibrated. Selecting as reference a sensor present in the third round (see
³⁴⁶ Fig. 7) minimizes the number of operations required to compute the offsets, thereby
³⁴⁷ reducing the associated uncertainty. Sensor 39645 was chosen as reference. Fig. 14-right
³⁴⁸ shows the distribution of the repeatability of the computed calibration constants, the
³⁴⁹ mean of which is slightly below the one obtained for the reference method. Thus, it
³⁵⁰ is confirmed that despite the higher number of intermediate sensors to relate any two
³⁵¹ sensors, the additional uncertainty introduced by the time walk correction makes the
³⁵² tree method superior to the reference method. Moreover, the reference method suffers a
³⁵³ —not yet known— systematic error associated to the time wall correction model.

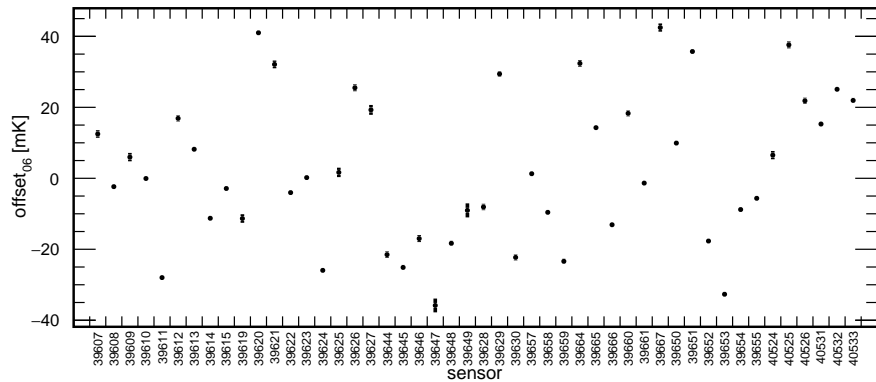


Figure 13: Offset of each sensor with respect to reference sensor 39606 using the reference method.

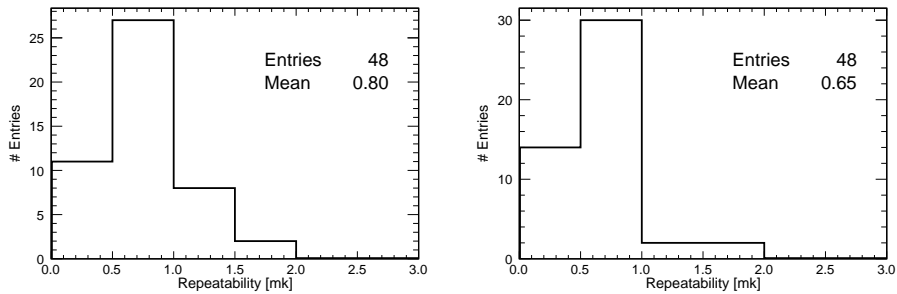


Figure 14: Left: repeatability distribution for the reference method. Right: repeatability distribution for tree method.

354 4.3.5. *Consistency cross-check and error estimation*

355 The uncertainties presented so far are generally below 1 mK and correspond to the
356 standard deviation of the four independent measurements of each calibration constant,
357 combined with the error propagation from the required corrections: time-walk correction
358 for the reference method, addition of calibration constants for the tree method, and the
359 uncorrected electronic residual offset common to both. These corrections likely include
360 unknown systematic effects impacting the final calibration constants. To estimate the
361 overall precision of the calibration, the following cross-check was performed. The cali-
362 bration strategy yields two independent calibration constants for each sensor—one from
363 the reference method and another from the tree method. For the sixteen sensors used in
364 the second round of the calibration tree, these two values are statistically independent
365 because they are derived from different sets of runs: the reference method relies solely
366 on first-round runs, while the tree method uses only second and third-round runs for
367 those sensors. Therefore, these sixteen sensors provide an effective basis for estimating
368 the calibration procedure's precision by comparing the results obtained from the two
369 methods.

370 By construction, the result of subtracting the calibration constants obtained in the
371 two methods should be compatible with the offset between sensors 39645 and 39606,
372 $\Delta T_{45,06} = \Delta T_{s,06} - \Delta T_{s,45} = T_{45} - T_{06}$, used as reference for the tree and reference
373 methods respectively. This offset is found to be -25.1 ± 0.7 mK by direct measurement
374 of the two sensors (see 10th column in Fig. 7 and 13). Fig. 15 shows this benchmark with
375 (left) and without (right) time walk corrections for the 16 sensors aforementioned, probing
376 the self-consistency of this correction. The standard deviation of this distribution, 2.4
377 mK, is an estimation of the quadratic sum of the total uncertainty of both calibrations.
378 Assuming that the reference sensor method has a larger uncertainty than the tree method
379 due to the time walk correction, an upper limit of 1.7 mK for the total error of the tree
380 method can be assumed. In the same way, this is the inferior limit for the total error of
381 the reference method. In both cases, these errors are less than half of what was originally
382 required for the TMS.

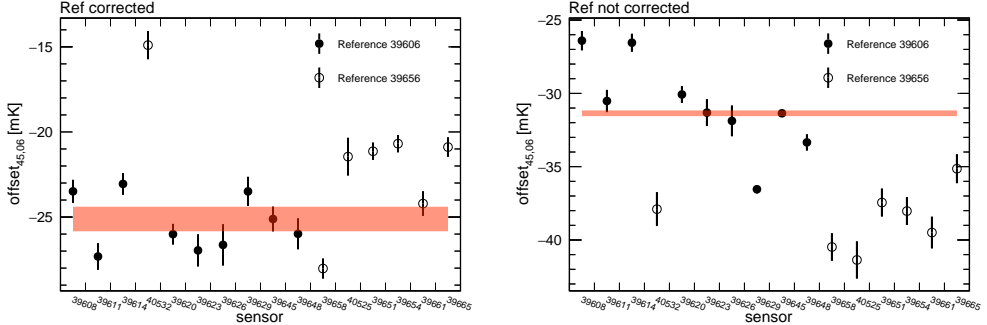


Figure 15: $\Delta T_{45,06}$ computed through all sensors of the second round of the calibration procedure. Left: applying corrections. Right: not applying corrections. A clear improvement is obtained using the corrections on the reference sensor. The red line represents the expected value of this calibration constant.

383 5. Re-calibration after ProtoDUNE-SP operation

384 After ProtoDUNE-SP decommissioning in 2020, temperature sensors were disconnected
 385 from the TGM and re-calibrated several times (see Table 1), using both LAr and LN2 as
 386 cryogenic liquid. The comparative analysis of those re-calibrations not only offers insights
 387 into the long-term stability of the sensors but also elucidates any potential dependencies
 388 on the choice of the cryogenic liquid. Although DUNE will use LAr, massive RTD
 389 calibration would benefit from using LN2, given its higher accessibility and lower cost.

date	cryogenic liquid	# sensors in capsule
March 2018	LAr	4
February 2022	LN2	14
March 2023	LN2	14
July 2023	LAr	14

Table 1: Calibration runs with indication of the date, the cryogenic liquid used and the number of sensors inside the capsule.

390 In this section, a description of the setup used for these new calibrations, the changes
 391 applied to the procedure as well as the results and conclusions of these calibrations are
 392 presented.

393 5.1. Evolution of the calibration setup

394 The Horizontal Drift Far Detector module will be equipped with over 500 precision sen-
 395 sors [4], making the use of the current calibration setup impractical, as it can accommo-

396 date only four sensors simultaneously. Significant modifications have been introduced in
397 order to increase this number to twelve, while maintaining the precision achieved during
398 the 2018 calibration campaign. This was accomplished by positioning sensors at the same
399 height, to avoid any potential vertical gradient, and following a cylindrical configuration,
400 under the assumption that convection inside the capsule has rotational symmetry. This
401 symmetry is also kept outside the capsule in all concentric cryogenic containers, having
402 added a fourth independent volume which should further reduce convection inside the
403 inner capsule. This notable advancement greatly streamlines the calibration process and
404 serves to reduce both statistical and systematic errors associated with the procedure.
405 Fig. 16 shows the different elements of the new calibration setup, which are described
406 below:

- 407 • A polystyrene box with dimensions $55 \times 35 \times 30 \text{ cm}^3$ and 4.5 cm thick walls with
408 a dedicated cover of the same material.
- 409 • Extruded polystyrene rectangles with a cylindrical hole of 12.5 cm diameter and
410 25 cm height, to conform the inner volume.
- 411 • A PTFE container with 12.5 cm diameter, 25 cm height and 2 mm thick walls to
412 fit in the hole left in the box. The approximate volume is 2 L.
- 413 • A 3D printed PLA cylinder with two independent concentric volumes, placed inside
414 the PTFE container.
- 415 • A cylindrical aluminum capsule to be placed in the inner volume of the PLA cylin-
416 der. It has 7 cm diameter, 14 cm height and 1 mm thick walls.
- 417 • A 3D printed PLA holder for 14 sensors, 12 of them forming a circle (the ‘corona’)
418 and the other 2 at the center, to be used as references. This support can be attached
419 to the aluminum capsule at a fixed height. Cables are naturally extracted from the
420 top of the assembly. A detailed view of this holder can be found in Fig. 16.
- 421 • The readout electronics, described in Sec. 3 has been retained from the previous
422 setup.

- 423 • A more cost effective cable with similar performance has been used. Produced by
 424 TempSens [24], it has four twisted cables instead of two separated twisted pairs
 425 and an additional Kapton insulation layer between the shielding mesh and the four
 426 conductors. Its diameter is 2.7 mm.

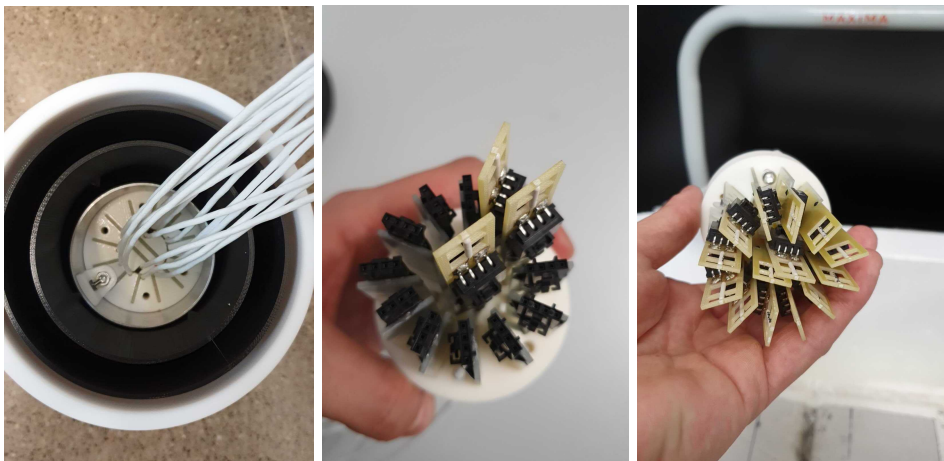


Figure 16: Left: The four concentric volumes of the calibration setup. Center: A view of one of the references and two corona sensors. Right: The 12 corona sensors plus the 2 references.

427 *5.2. Calibration procedure*

428 The sensor support was originally designed to accommodate two reference sensors in
 429 the center (see Fig. 16), enabling both the reference and tree calibration methods.
 430 However, it was soon observed that temperature variations between corona and reference
 431 sensors were significantly larger than those between any two corona sensors. This effect
 432 is attributed to the convection pattern inside the capsule, which is expected to have
 433 rotational invariance, and hence favour sensors disposed following a cylindrical symmetry.
 434 This can be observed in Fig. 17-left, where the offset between two corona sensors is
 435 nearly constant in time in four independent measurements, and in Fig. 17-right, where
 436 the offset between a corona and a reference sensor shows a more chaotic behaviour.
 437 Consequently, only the ‘tree’ calibration method was considered during the calibrations
 438 after ProtoDUNE-SP decommissioning.

439 The new calibration tree, shown in Fig. 18, contemplates four 12-sensors sets in the
 440 first round, and a unique second round with three promoted sensors from each of the

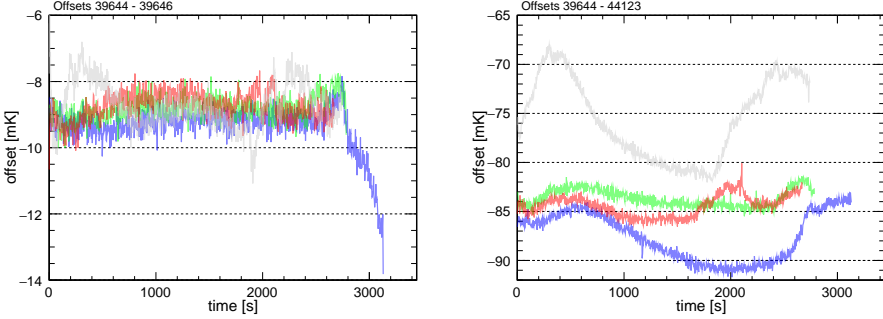


Figure 17: Left: The 4 measured offsets between two arbitrary sensors in the corona. Right: The 4 measured offsets between a sensor in the corona and one of the references, at the center.

441 sets in the first round. With this scheme, promoted sensors only suffer 8 baths, avoiding
 442 the necessity of a time-walk correction.

443 The experimental procedure is similar to the one presented in Sec. 4. Two small
 444 variations were introduced. First, the several concentric containers are cooled down
 445 for 40 minutes before introducing the aluminium capsule for the first time in a day,
 446 slightly improving the results of the first calibration run. Second, the warm up process
 447 is accelerated using a heat gun, avoiding the use of water.

448 5.3. Calibration results

449 A sensor from the second round is chosen as the reference, as this minimizes the number of
 450 operations required for the non-promoted sensors. Since each set includes three promoted
 451 sensors, there are three **linearly independent** ways to compute the offset relative to the
 452 reference for the nine non-promoted sensors in that set. The calibration constant for these
 453 sensors is calculated as the weighted average of the three “paths”, while the uncertainty
 454 is taken as the standard deviation of these three values. The offset error used in the
 455 weighted average for each of the three paths and is computed by quadratically adding
 456 the individual uncertainties on each of the terms contributing to that specific offset. For
 457 the remainder of the analysis, sensor 40525 is used as the absolute reference.

458 Fig. 19 shows the distribution of the repeatability (defined in Sec. 4.3.1) for the three
 459 new calibrations mentioned in Table 1. **AÑADIR AQUÍ EL PORQUÉ LAR2023 TIENE**
 460 **47 entries.** In all three cases the uncertainty is slightly above 1 mK. Mean values are
 461 larger than the ones obtained in the 2018 calibration campaign. This is attributed to

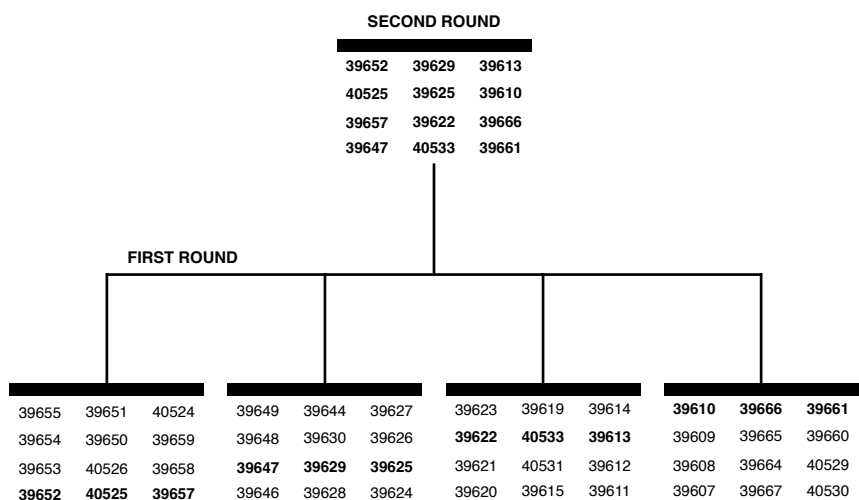


Figure 18: Schematic of the calibration sequence used with the new setup. Each of the sets contains 12 sensors, all of them placed in the corona, plus 2 references at the center. Sensors in bold in the first round are promoted to the second round.

462 the increased capsule size and the larger distance between sensors inside the capsule.
 463 This hypothesis is supported by Fig. 20, showing the repeatability as a function of the
 464 distance to the reference sensor in the corona for a particular measurement. However,
 465 there is no substantial difference between the repeatability obtained for LN2 and LAr
 466 calibrations.

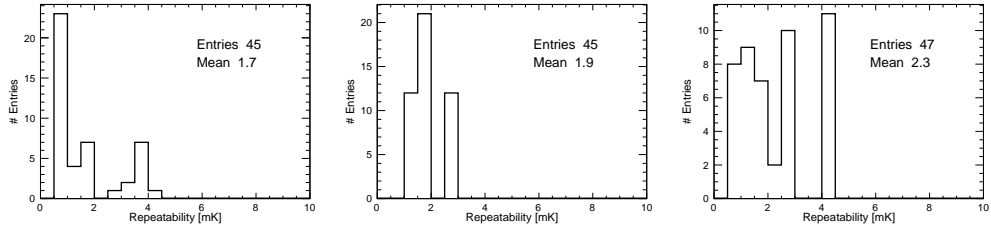


Figure 19: Repeatability distribution for the new calibrations. Left: LN2-2022. Middle: LN2-2023, Right:LAr-2023

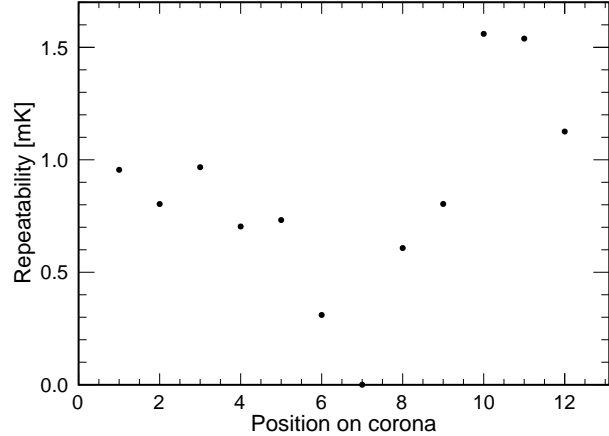


Figure 20: Repeatability as a function of position in the corona for the first set of the LAr-2023 calibration campaign. Sensor in position 7 is taken as reference.

467 Comparison between LN2 and LAr calibrations can also be used to understand the
 468 dependence of the calibration constants on the absolute temperature. This is shown
 469 in Fig. 21 along with other comparisons between calibration campaigns. The standard
 470 deviation of the distribution is lower when comparing two calibrations in the same liquid
 471 (LN2 in this case). However no bias is observed when comparing calibrations in two

472 different liquids, indicating that offsets are insensitive to a 10 K variation in absolute
 473 temperature.

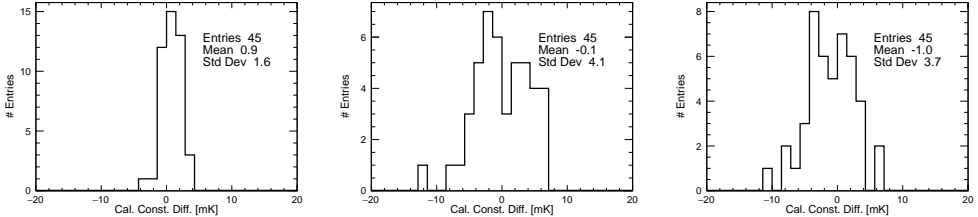


Figure 21: Difference between offsets for two calibrations. Left: LN2-2022 and LN2-2023. Middle: LN2-2022 and LAr-2023. Right: LN2-2023 and LAr-2023.

474 Ageing and long term stability have also been addressed. The left panel of Fig. 21
 475 shows no difference between the offsets calculated in LN2 with a delay of one year. A bet-
 476 ter understanding of this effect is achieved by comparing with the LAr-2018 calibration,
 477 as shown in the next section.

478 5.4. Comparison between new and old calibrations

479 Fig. 22 shows the distribution of the offset difference between the LAr-2018 and LAr-
 480 2023 calibrations. The mean of the distribution is -0.1 ± 0.6 mK, excluding any relevant
 481 systematic drift. The standard deviation of the distribution, 4.0 mK, is only slightly
 482 larger than the ones obtained in the comparison between newer calibrations, which could
 483 be due to the unknown contribution of the uncorrected readout offsets, pointing to small
 484 or non-existing ageing effects. This can also be observed in Table 2, summarizing the
 485 results of all possible comparisons between calibration campaigns, showing the mean and
 486 standard deviation of those comparisons. The lowest standard deviation, 1.6 mK, is
 487 obtained for the LN2-2022 to LN2-2023 combination, which is somehow expected since
 488 i) the cryogenic liquid is the same, ii) ageing should be small since there is only one year
 489 difference and iii) having use the same readout channels, readout offsets cancel out.
 490 The difference between the constants obtained in two calibration campaigns can be used
 491 to estimate the total calibration error. Since ProtoDUNE Horizontal Drift (ProtoDUNE-
 492 HD), the next iteration of the ProtoDUNE-SP detector, and DUNE will use LAr, the
 493 best estimation of the error would come from a LAr to LAr comparison close in time to
 494 the actual detector running. Being this combination not available, three other combina-

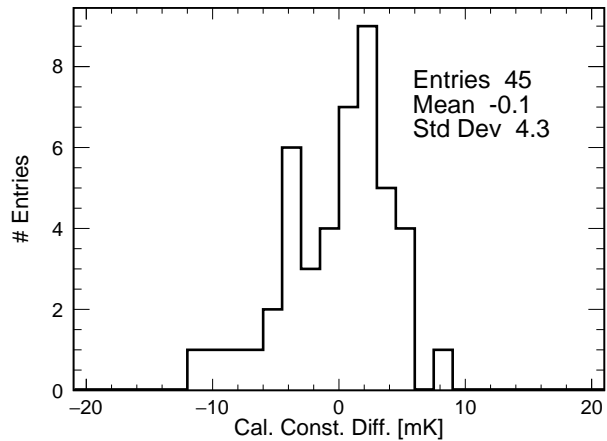


Figure 22: Difference between offsets for LAr-2018 and LAr-2023 calibration campaigns.

	LAr-2018	LN2-2022	LN2-2023	LAr-2023
LAr-2018	-	0.0, 3.5	0.9, 3.9	-0.1, 4.3
LN2-2022	-	-	0.9, 1.6	-0.1, 4.1
LN2-2023	-	-	-	-1.0, 3.7
LAr-2023	-	-	-	-

Table 2: Mean and standard deviation of the difference between the calibration constants obtained in two calibration campaigns.

495 tions can be used. The comparison between the LN2 calibrations from 2022 and 2023
496 yields a standard deviation of 1.6 mK, which should represent the quadratic sum of the
497 individual calibration errors. Assuming equal errors for both campaigns, this implies a
498 single calibration error of approximately 1.13 mK. In this case, readout channel offsets
499 cancel out, although real fluctuations in those offsets still contribute to the estimated
500 single calibration error. The comparison between LAr calibrations from 2018 and 2023
501 provides further insight, with a standard deviation of 4.3 mK, corresponding to a sin-
502 gle calibration error of about 3.0 mK. However, this value includes uncorrected readout
503 offsets as well as potential effects from sensor ageing. Finally, comparing the new LAr
504 and LN2 calibration campaigns avoids issues related to readout offsets and ageing but
505 may be affected by the differences in cryogenic liquids. These comparisons yield a similar
506 standard deviation around 3.8 mK, implying a single calibration error of approximately
507 2.7 mK. This value thus establishes an upper limit on the LAr calibration error. In
508 summary, the individual calibration error in LAr is estimated to lie between 1.6 and
509 3.0 mK. This range is consistent with an independent estimate of 1.7 mK obtained using
510 a different method for the LAr-2018 calibration (see Sec. 4.3.5).

511 6. Conclusions

512 The DUNE experiment will require the construction and operation of the largest cryostats
513 ever used in a particle physics experiment. This makes the continuous measurement of
514 temperature gradients in liquid argon crucial for monitoring the stability of the cryogenics
515 system and for detector calibration. R&D on the calibration of RTD probes started in
516 2017, leading to promising results for sensors installed in the DUNE prototype at CERN.

517 The first setup proved the viability of the method, obtaining a calibration error of 1.7
518 mK. A key component was the readout electronics, with an intrinsic resolution better
519 than 0.5 mK in the comparison between two channels. The mechanics was also crucial,
520 with several insulation layers consisting of independent concentric volumes, ensuring
521 minimal convection in the inner volume. Sensors were contained in an aluminium capsule,
522 enabling slow cool-down and warm-up processes, found to be fundamental to guarantee
523 the integrity of the sensors and to minimize the effect of ageing.

524 The calibration system was later enhanced to accommodate the large-scale calibration

525 required for the DUNE detectors. The capacity of the inner capsule was increased from
526 4 to 14 sensors, while improvements were made to the insulation and symmetry of the
527 system to minimize temperature differences between sensors. The new system has slightly
528 worst repeatability for sensors in the same set, but reduces the statistical and systematic
529 errors associated to the calibration tree, needed to relate any two sensors in different
530 calibration sets. Calibration with the new setup has achieved a precision in the range of
531 1.6-3.0 mK, substantially better than the 5 mK DUNE requirement.

532 Another difference between the new and old calibrations is the use of a different
533 cryogenic liquid. While DUNE will use LAr, LN2 is cheaper, simplifying the process of
534 massive calibration for DUNE detectors. The 10 K difference between those liquids has
535 a minimal effect on the calibration constants.

536 A comparison of the four calibration campaigns has provided valuable insights into
537 aging effects, with no evidence of RTD aging observed over a five-year period. This
538 highlights the stability and reliability of the PT-102-based system.

539 7. Acknowledgments

540 The present research has been supported and partially funded by Conselleria d’Innovació,
541 Universitats, Ciència i Societat Digital, by the Fundación ‘La Caixa’, and by MICINN.
542 The authors would also like to thank all the people involved in the installation,
543 commissioning and operation of ProtoDUNE-SP, specially to Stephen Ponders.

544 References

- 545 [1] Abi, B., et al. (DUNE), 2017. The Single-Phase ProtoDUNE Technical Design Report
546 [arXiv:1706.07081](https://arxiv.org/abs/1706.07081).
- 547 [2] Abi, B., et al. (DUNE), 2020a. Deep Underground Neutrino Experiment (DUNE), Far Detector
548 Technical Design Report, Volume I Introduction to DUNE. JINST 15, T08008. doi:10.1088/
549 1748-0221/15/08/T08008, [arXiv:2002.02967](https://arxiv.org/abs/2002.02967).
- 550 [3] Abi, B., et al. (DUNE), 2020b. Deep Underground Neutrino Experiment (DUNE), Far Detector
551 Technical Design Report, Volume II: DUNE Physics [arXiv:2002.03005](https://arxiv.org/abs/2002.03005).
- 552 [4] Abi, B., et al. (DUNE), 2020c. Deep Underground Neutrino Experiment (DUNE), Far Detector
553 Technical Design Report, Volume IV: Far Detector Single-phase Technology. JINST 15, T08010.
554 doi:10.1088/1748-0221/15/08/T08010, [arXiv:2002.03010](https://arxiv.org/abs/2002.03010).
- 555 [5] Abi, B., et al. (DUNE), 2020d. First results on ProtoDUNE-SP liquid argon time projection
556 chamber performance from a beam test at the CERN Neutrino Platform. JINST 15, P12004.
557 doi:10.1088/1748-0221/15/12/P12004, [arXiv:2007.06722](https://arxiv.org/abs/2007.06722).
- 558 [6] Abi, B., et al. (DUNE), 2020e. Long-baseline neutrino oscillation physics potential of the DUNE
559 experiment. Eur. Phys. J. C 80, 978. doi:10.1140/epjc/s10052-020-08456-z, [arXiv:2006.16043](https://arxiv.org/abs/2006.16043).
- 560 [7] Abi, B., et al. (DUNE), 2021a. Prospects for beyond the Standard Model physics searches
561 at the Deep Underground Neutrino Experiment. Eur. Phys. J. C 81, 322. doi:10.1140/epjc/
562 s10052-021-09007-w, [arXiv:2008.12769](https://arxiv.org/abs/2008.12769).

- 563 [8] Abi, B., et al. (DUNE), 2021b. Supernova neutrino burst detection with the Deep Under-
 564 ground Neutrino Experiment. *Eur. Phys. J. C* 81, 423. doi:10.1140/epjc/s10052-021-09166-w,
 565 arXiv:2008.06647.
- 566 [9] Abud, A.A., et al. (DUNE), 2022. Design, construction and operation of the ProtoDUNE-SP Liquid
 567 Argon TPC. *JINST* 17, P01005. doi:10.1088/1748-0221/17/01/P01005, arXiv:2108.01902.
- 568 [10] Acciarri, R., et al. (MicroBooNE), 2017. Design and Construction of the MicroBooNE Detector.
 569 *JINST* 12, P02017. doi:10.1088/1748-0221/12/02/P02017, arXiv:1612.05824.
- 570 [11] Adamowski, M., et al., 2014. The Liquid Argon Purity Demonstrator. *JINST* 9, P07005. doi:10.
 571 1088/1748-0221/9/07/P07005, arXiv:1403.7236.
- 572 [12] Adams, D.L., et al., 2020. Design and performance of a 35-ton liquid argon time projection chamber
 573 as a prototype for future very large detectors. *JINST* 15, P03035. doi:10.1088/1748-0221/15/03/
 574 P03035, arXiv:1912.08739.
- 575 [13] Amerio, S., et al. (ICARUS), 2004. Design, construction and tests of the ICARUS T600 detector.
 576 *Nucl. Instrum. Meth. A* 527, 329–410. doi:10.1016/j.nima.2004.02.044.
- 577 [14] Axon, . Axon custom cables. URL: https://www.axon-cable.com/en/00_home/00_start/00_index.aspx. last visited: 2022-10-01.
- 578 [15] application bulletin, B.B., . Implementation and applications of current sources and current re-
 579 ceivers. URL: <https://www.ti.com/lit/an/sboa046/sboa046.pdf?ts=1712062207089>. last visited:
 580 2024-04-02.
- 581 [16] Chojnacki, E., 2009. A Multiplexed RTD Temperature Map System for Multi-Cell SRF Cavities,
 582 in: SRF2009, p. 232.
- 583 [17] García-Peris, M.A., 2018. ProtoDUNE T-Gradient development and calibration. Master's thesis.
 584 Valencia U. doi:10.2172/1780813.
- 585 [18] Hahn, A., Adamowski, M., Montanari, D., Norris, B., Reichenbacher, J., Rucinski, R., Stewart,
 586 J., Tope, T. (LBNE), 2016. The LBNE 35 Ton Prototype Cryostat, in: 2014 IEEE Nuclear Sci-
 587 ence Symposium and Medical Imaging Conference and 21st Symposium on Room-Temperature
 588 Semiconductor X-ray and Gamma-ray Detectors. doi:10.1109/NSSMIC.2014.7431158.
- 589 [19] Instruments, N., a. Compactrio systems. URL: <https://www.ni.com/es/shop/compactrio.html>.
 590 last visited: 2024-04-02.
- 591 [20] Instruments, N., b. Ni-9238. URL: <https://www.ni.com/es-es/shop/model/ni-9238.html>. last
 592 visited: 2024-04-02.
- 593 [21] LakeShore, . Platinum sensors applications. URL: <https://www.lakeshore.com/products/categories/overview/temperature-products/cryogenic-temperature-sensors/platinum>. last
 594 visited: 2023-05-18.
- 595 [22] Minco, . Resistance thermometry. URL: <https://www.minco.com/wp-content/uploads/Resistance-Thermometry.pdf>. last visited: 2023-05-18.
- 596 [23] Tektronix, . Keithley 2001 digit high performance multimeter. URL: https://download.tek.com/datasheet/1KW-73954-1_2001-2002_DMM_Datasheet_080323.pdf. last visited: 2024-04-02.
- 597 [24] TempSens, . Rtd cables. URL: <https://tempsens.com/catalog/cables-wires/rtd-triad-cables.html>. last visited: 2024-03-15.
- 598 [25] Xiao, Y. (DUNE), 2021. Purity monitoring for ProtoDUNE-SP. *J. Phys. Conf. Ser.* 2156, 012211.
 599 doi:10.1088/1742-6596/2156/1/012211.
- 600
- 601
- 602
- 603
- 604